

# SCISSR: Scribble-Conditioned Interactive Surgical Segmentation and Refinement

Haonan Ping<sup>1</sup>, Jian Jiang<sup>1</sup>, Cheng Yuan<sup>1</sup>, Qizhen Sun<sup>1</sup>, Lv Wu<sup>1</sup>, and Yutong Ban<sup>1</sup>

Global College, Shanghai Jiao Tong University, Shanghai, China  
yban@sjtu.edu.cn

**Abstract.** Accurate segmentation of tissues and instruments in surgical scenes is annotation-intensive due to irregular shapes, thin structures, specularities, and frequent occlusions. While SAM models support point, box, and mask prompts, points are often too sparse and boxes too coarse to localize such challenging targets. We present SCISSR, a scribble-promptable framework for interactive surgical scene segmentation. It introduces a lightweight Scribble Encoder that converts freehand scribbles into dense prompt embeddings compatible with the mask decoder, enabling iterative refinement for a target object by drawing corrective strokes on error regions. Because all added modules (the Scribble Encoder, Spatial Gated Fusion, and LoRA adapters) interact with the backbone only through its standard embedding interfaces, the framework is not tied to a single model: we build on SAM 2 in this work, yet the same components transfer to other prompt-driven segmentation architectures such as SAM 3 without structural modification. To preserve pre-trained capabilities, we train only these lightweight additions while keeping the remaining backbone frozen. Experiments on EndoVis 2018 demonstrate strong in-domain performance, while evaluation on the out-of-distribution CholecSeg8k further confirms robustness across surgical domains. SCISSR achieves 95.41% Dice on EndoVis 2018 with five interaction rounds and 96.30% Dice on CholecSeg8k with three interaction rounds, outperforming iterative point prompting on both benchmarks.

**Keywords:** Interactive segmentation · Scribble annotation · Surgical scene segmentation

## 1 Introduction

Pixel-level segmentation of surgical scenes is essential for intraoperative guidance and postoperative analysis, yet large-scale annotation is expensive due to cluttered, deformable, and overlapping anatomy and tools. Interactive segmentation reduces this cost: the annotator provides a coarse prompt, receives a predicted mask, and refines it through further interaction.

Foundation models such as SAM [9], SAM 2 [16], and SAM 3 [2] have made prompt-based segmentation practical, and medical adaptations [14,3] extend their reach. However, the supported prompt types (points, boxes, masks, and

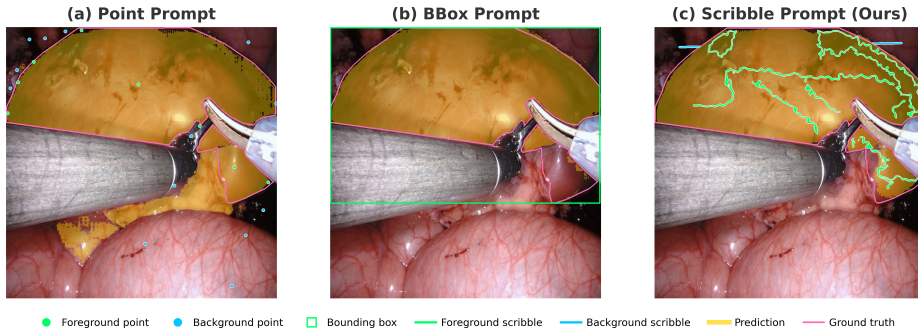


**Fig. 1.** Motivation for scribble prompts. Points provide sparse cues and boxes enclose large background regions, while scribbles outline the target with dense spatial coverage.

text) each have limitations in surgical scenes: bounding boxes cover large background areas around curved vessels or thin instruments, point clicks require many rounds for complex morphologies, and SAM 3’s text prompts address concept-level recognition rather than instance-level delineation. As shown in Fig. 1, scribbles offer a natural middle ground: they trace the target with dense spatial coverage while requiring only slightly more effort than a click.

Prior interactive methods are predominantly click-based [26,18,19,12] (including medical variants [21,13]), and most surgical adaptations of SAM/SAM 2 retain point/box prompting [14,3,29,8,28,27]. In contrast, ScribblePrompt [23] is primarily developed for intensity-normalized (often single-channel) biomedical images and does not leverage SAM 2’s memory bank, while other works use scribbles only as weak supervision [10,20,30].

We present SCISSR, which equips SAM 2 with scribble-conditioned multi-round refinement for surgical scene segmentation. Our contributions are three-fold: (1) a lightweight Scribble Encoder that maps freehand scribbles to dense prompt embeddings, enabling iterative correction via successive strokes; (2) an architecture-agnostic design where the Scribble Encoder, Spatial Gated Fusion, and LoRA [6] adapters attach through standard embedding interfaces, making the approach transferable to architectures such as SAM 3; and (3) evaluation on both EndoVis 2018 and the out-of-distribution CholecSeg8k, confirming that scribble prompting generalizes across surgical domains (95.41% Dice on EndoVis 2018, 96.30% on CholecSeg8k).

## 2 Method

### 2.1 Overview

Fig. 2 illustrates SCISSR, a scribble-promptable framework for interactive refinement. Although we instantiate SCISSR on SAM 2 in this work, every added component communicates with the backbone exclusively through its standard embedding interfaces (dense prompt embeddings, memory-attention queries, and

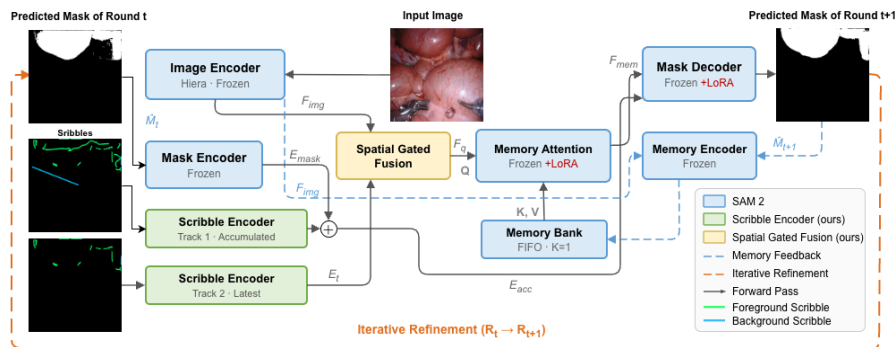


**Fig. 2.** Overview of SCISSR. Track 1 encodes all accumulated scribbles as dense prompt embeddings for the mask decoder; Track 2 encodes only the latest correction and injects it into the Memory Attention query via Spatial Gated Fusion. The mask is iteratively refined across rounds ( $R_0 \rightarrow R_1 \rightarrow R_2 \rightarrow \dots$ ). Blue: frozen SAM 2 components; green/yellow: trainable components.

LoRA-injected projections). Given an image  $I \in \mathbb{R}^{3 \times H \times W}$  and a two-channel scribble map  $S \in \{0, 1\}^{2 \times H \times W}$  (positive/foreground and negative/background), we freeze SAM 2’s image encoder and introduce three lightweight components: (i) a Scribble Encoder that converts  $S$  into dense prompt embeddings, (ii) a Spatial Gated Fusion (SGF) module that injects the *latest* correction into the memory query, and (iii) a memory-driven iterative refinement loop that repurposes SAM 2’s temporal memory for multi-round correction on a single image.

A key design is a **dual-track** scribble pathway. **Track 1 (Accumulated  $\rightarrow$  Dense Prompt)**: the union of scribbles across rounds is encoded and added to the mask decoder’s dense prompt embedding, preserving the user’s full intent. **Track 2 (Latest  $\rightarrow$  Memory Query)**: only the current round’s scribble is encoded and fused into the query features of Memory Attention through SGF, encouraging attention to focus on newly corrected regions.

## 2.2 Scribble Encoder

The Scribble Encoder follows SAM 2’s mask-prompt downscaling design. We resize  $S$  to  $256 \times 256$ , apply two stride-2 convolution blocks ( $2 \times 2 \text{ Conv} \rightarrow \text{LayerNorm2d} \rightarrow \text{GELU}$ ), and a final  $1 \times 1$  projection to  $D=256$ , producing a dense embedding  $E_S \in \mathbb{R}^{256 \times 64 \times 64}$  aligned with SAM 2’s image-embedding resolution. We zero the embedding when the channel input is empty.

## 2.3 Spatial Gated Fusion

The Spatial Gated Fusion (SGF) module injects the latest scribble into the query features of Memory Attention. A binary hard gate  $g_h \in \{0, 1\}$  disables the fusion branch when no scribble is provided. When active, image features

$F \in \mathbb{R}^{D \times H' \times W'}$  and scribble embedding  $E_S$  are concatenated and processed by a spatial mixing operator:

$$\text{SpatialMix}(\text{Concat}(F, E_S)) = \phi_{\text{dw}}\left(\phi_{1 \times 1}(\text{Concat}(F, E_S))\right),$$

where  $\phi_{1 \times 1}$  reduces  $2D$  channels back to  $D$  (with GroupNorm and GELU), and  $\phi_{\text{dw}}$  is a  $7 \times 7$  depthwise-separable convolution block that propagates the scribble signal spatially. A learnable scalar  $\alpha$  (initialized to zero) controls the fusion strength:

$$F' = F + \alpha \cdot g_h \cdot \text{SpatialMix}(\text{Concat}(F, g_h \cdot E_S)). \quad (1)$$

Because  $\alpha$  is initialized to zero, SGF acts as an identity mapping at the start of training and leaves the pretrained features unchanged.

## 2.4 Memory-Driven Iterative Refinement

SCISSR repurposes SAM 2’s temporal memory for multi-round correction on a single image. Image features are computed once and cached. Track 1 accumulates all scribbles (channel-wise maximum) as a dense prompt, while Track 2 injects only the latest correction via SGF. The Memory Bank retains only the previous round’s encoded features as a single memory entry for cross-attention. This suffices because Track 1 already preserves the full interaction history. The complete pseudocode is given in Algorithm 1 (Appendix A).

## 2.5 Toggleable LoRA for Scribble Adaptation

We keep SAM 2’s image encoder entirely frozen. LoRA adapters [6] are inserted into the query and value projections of all multi-head attention layers in the **mask decoder** and **memory attention** module, with  $B$  zero-initialized so that  $\Delta W=0$  at the start of training. Importantly, these adapters are toggleable: we enable them for scribble-conditioned refinement and can disable them for standard video propagation by setting the LoRA scaling to zero.

## 2.6 Training Pipeline

Training proceeds in two stages. **Stage 1** trains the Scribble Encoder and mask decoder LoRA without memory or SGF, using multi-round ( $T=3$ ) scribble-to-mask prediction with oracle corrections. **Stage 2** jointly trains all four components (Scribble Encoder, SGF, mask decoder LoRA, Memory Attention LoRA) with the full iterative pipeline. For each training sample, we unroll  $T=3$  rounds: initial scribbles at  $t=0$  and error-driven corrective scribbles for  $t>0$  (Sec. 2.7).

The loss at each round combines Focal Loss and Dice Loss with linearly increasing round weights  $w_t = t + 1$ :

$$\mathcal{L}_{\text{total}} = \sum_{t=0}^{T-1} \frac{w_t}{\sum_j w_j} \left[ 20 \cdot \mathcal{L}_{\text{focal}}(\hat{M}_t, M^*) + \mathcal{L}_{\text{dice}}(\hat{M}_t, M^*) \right]. \quad (2)$$

## 2.7 Scribble Generation

Since large-scale scribble annotations are unavailable, we synthesize scribbles from ground-truth masks. An Adaptive Scribble Generator selects one of four types per connected component based on geometric cues: *centerline* (skeleton strokes), *wave skeleton* (oscillating centerline), *contour* (boundary-following with inward offset), and *line* (negative strokes for false positives), with mild spatial perturbations to mimic freehand variability. For correction rounds, false negatives receive positive geometry-aware scribbles and false positives receive negative cross-out strokes [23].

## 3 Experiments

### 3.1 Datasets and Metrics

We evaluate on two laparoscopic surgical datasets. **EndoVis18** [1] provides 15 training and 4 test sequences of robotic nephrectomy (2,235 / 999 frames, 10 foreground classes, 4,616 test samples). As the model is trained on this dataset, it serves as the in-distribution (ID) benchmark. **CholecSeg8k** [5] provides 8,080 cholecystectomy frames with 12 foreground classes; we hold out 1,679 frames (8,800 test samples). No CholecSeg8k data is seen during training, making it an out-of-distribution (OOD) benchmark. We report IoU and Dice (%) per round as **sample-average** ( $mIoU/mDice$ ) and **class-average** ( $cIoU/cDice$ );  $R_k$  denotes the prediction after  $k$  refinement rounds.

### 3.2 Implementation Details

We build on SAM 2 Tiny as the backbone. LoRA adapters with rank  $r = 8$  and scaling factor  $\alpha/r = 2$  are inserted into the query and value projections of all multi-head attention layers in the mask decoder and Memory Attention module; the image encoder remains entirely frozen. We train for 10 epochs using the AdamW optimizer with a weight decay of 0.01, a batch size of 2, and automatic mixed-precision training (AMP) on a single NVIDIA RTX 4090 (24GB), with learning rates of  $1 \times 10^{-4}$  for Stage-2 newly added modules and  $1 \times 10^{-5}$  for Stage 1 modules.

### 3.3 Comparison with Baselines

We compare against point-based iterative methods (SAM 2 Tiny and SAM 3, each with 1 pt/CC and 10 pt/ch protocols), single bounding box baselines (SAM 2 Tiny, SAM 3, and MedSAM2 [15]), all evaluated under the same fixed-round automated protocol (Sec. 3.4). 1 pt/CC uses one click per error-region connected component (at its centroid), whereas 10 pt/ch provides up to 10 positive and 10 negative clicks per round (prioritizing connected-component centroids when selecting points).

**Table 1.** Comparison on EndoVis 2018 (ID,  $N=4,616$ ) and CholecSeg8k (OOD,  $N=8,800$ ). mIoU / mDice (%).  $Rk$ : after  $k$  refinement rounds. N/A: not applicable.

Method	EndoVis 2018 (ID)						CholecSeg8k (OOD)			
	<b>R0</b>		<b>R2</b>		<b>R4</b>		<b>R0</b>		<b>R2</b>	
	mIoU	mDice	mIoU	mDice	mIoU	mDice	mIoU	mDice	mIoU	mDice
<i>Point Prompt Baselines</i>										
SAM2 Tiny (1pt/CC)	56.47	68.31	62.73	73.77	55.83	66.73	62.18	72.30	62.18	73.44
SAM2 Tiny (10pt/ch)	62.09	73.93	71.17	80.39	63.15	72.08	67.65	77.84	75.02	83.18
SAM3 (1pt/CC)	57.29	69.18	59.70	70.36	51.32	60.24	56.74	67.24	52.62	61.69
SAM3 (10pt/ch)	58.69	71.09	62.52	72.59	40.38	47.95	57.36	69.23	68.86	78.69
<i>Bounding Box Baselines</i>										
SAM 2 Tiny (BBox)	64.11	73.23	N/A		N/A		76.22	84.62	N/A	
SAM 3 (BBox)	69.13	77.97	N/A		N/A		77.85	85.78	N/A	
MedSAM2 (BBox)	45.87	54.54	N/A		N/A		76.74	82.69	N/A	
<i>Supervised Baselines (trained on EndoVis 2018)</i>										
U-Net [17]	50.70	61.50	N/A		N/A		N/A		N/A	
UPerNet [24]	58.40	66.80	N/A		N/A		N/A		N/A	
HRNet [22]	63.30	71.80	N/A		N/A		N/A		N/A	
SegFormer [25]	63.00	71.90	N/A		N/A		N/A		N/A	
SegNeXt [4]	64.30	72.50	N/A		N/A		N/A		N/A	
STSwIn-CL [7]	63.60	72.00	N/A		N/A		N/A		N/A	
LSKA-Net [11]	66.20	75.30	N/A		N/A		N/A		N/A	
TAFPNNet [27]	82.60	89.90	N/A		N/A		N/A		N/A	
<i>Ours (Scribble Prompt)</i>										
SCISSR (Adaptive)	75.72	85.18	88.32	93.49	90.18	94.61	83.42	90.24	92.30	95.82
SCISSR (Contour)	79.42	87.63	90.03	94.51	<b>91.60</b>	<b>95.41</b>	84.25	90.75	<b>93.22</b>	<b>96.30</b>
SCISSR (Wave)	73.55	83.66	88.69	93.72	90.36	94.39	82.49	89.57	92.04	95.67
SCISSR (Centerline)	74.16	84.13	85.31	91.58	86.55	92.30	83.00	90.00	90.80	94.88

Table 1 reports results on both datasets. On EndoVis 2018, the contour model reaches 91.60% mIoU at R4, while point-based methods often degrade with more rounds, with R4 metrics generally lower than R2. Bounding box and supervised baselines do not support iterative refinement and are therefore marked N/A for later rounds. On CholecSeg8k (OOD), our adaptive model reaches 92.30% mIoU at R2 without any CholecSeg8k training data, exceeding box baselines (76–78% mIoU) by over 14 pp. Although our model is also trained exclusively on EndoVis 2018, it generalizes well to the unseen CholecSeg8k domain, whereas supervised baselines trained on the same data are not directly applicable to CholecSeg8k due to differences in the label set. Class-average breakdowns and additional OOD tables are provided in Appendix B.

**Convergence efficiency.** For interactive annotation, the practical value of a method depends on how quickly it reaches acceptable quality. Table 2 summarizes success rates and mean rounds on EndoVis 2018, showing that SCISSR consistently converges faster and succeeds more often than point-based baselines across Dice thresholds.

**Per-class analysis.** Fig. 3 shows per-class results. On EndoVis 2018, classes with irregular geometry benefit most: *suturing needle* (+24.92 pp), *covered kidney* (+22.15 pp), and *wrist* (+14.16 pp). On CholecSeg8k (OOD), the model generalizes across all 12 classes without any CholecSeg8k training data. Full per-class tables for all strategies and baselines are in Appendix C.

**Table 2.** Convergence efficiency on EndoVis 2018 ( $N=4,616$ ). Success: % of masks reaching the Dice threshold within 4 rounds.

Method	Dice $\geq$	Success (%)	Mean Rnd	Cumulative % by round				
				R0	R1	R2	R3	R4
SAM2 Tiny (1pt/CC)	0.75	75.5	1.51	50.3	66.4	72.2	74.5	75.5
	0.85	56.4	1.76	31.2	45.3	51.6	54.7	56.4
	0.90	40.9	1.89	19.5	31.2	36.9	39.4	40.9
SAM3 (1pt/CC)	0.75	71.6	1.44	51.9	64.2	68.4	70.4	71.6
	0.85	52.9	1.75	30.1	42.2	48.4	51.2	52.9
	0.90	39.7	2.04	17.6	27.8	34.2	37.8	39.7
SCISSR (Adaptive)	0.75	<b>99.0</b>	<b>1.37</b>	70.2	92.9	97.3	98.5	99.0
	0.85	<b>94.7</b>	<b>1.68</b>	48.4	81.5	90.7	93.4	94.7
	0.90	<b>87.7</b>	<b>1.98</b>	33.3	66.9	79.2	85.2	87.7

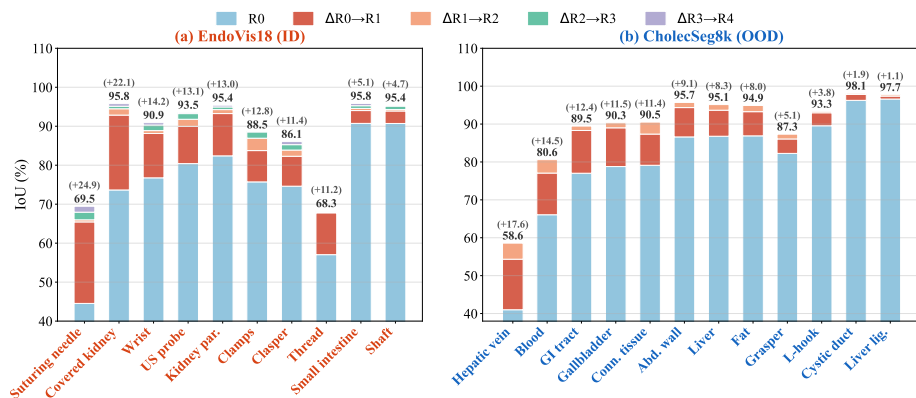


**Fig. 3.** Per-class IoU with incremental refinement gains. (a) EndoVis 2018 (contour,  $R0 \rightarrow R4$ ). (b) CholecSeg8k (OOD,  $R0 \rightarrow R2$ ). Numbers at bar tops: final IoU and total gain.

### 3.4 Automated Evaluation Protocol

We use an automated protocol to simulate iterative interaction. An initial scribble is generated from the ground-truth mask (Sec. 2.7); the model predicts a mask and, if  $\text{IoU} < \tau$ , corrective scribbles are generated on error regions for the next round, repeating for at most  $T$  rounds. Point-click baselines follow the same protocol with clicks at the center of each error-region connected component.

**Limitations of point prompts.** One might attribute our gains to scribbles containing more labeled pixels. However, for point prompting, both 1pt/CC and the denser 10pt/ch protocol in Table 1 can degrade as rounds increase, despite receiving more clicks. This indicates that point quantity alone is insufficient; the structured spatial layout of scribbles provides richer shape and boundary cues than isolated clicks (see Appendix D for a detailed density analysis).

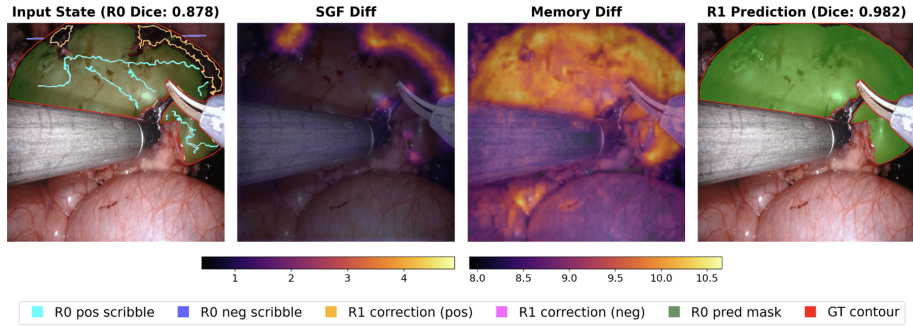


**Fig. 4.** Qualitative visualization of feature changes from R0→R1: SGF-induced query modification ( $|F_q - F_{img}|$ ) and Memory-induced update ( $|F_{mem} - F_{img}|$ ), alongside input scribbles and the refined R1 prediction.

**Table 3.** Component ablation on EndoVis 2018. All metrics (%) are sample-average (m) and class-average (c). Each row adds one module to the previous configuration.

Configuration	R0				R1				R2			
	mIoU	mDice	cIoU	cDice	mIoU	mDice	cIoU	cDice	mIoU	mDice	cIoU	cDice
Baseline	69.88	80.73	69.68	80.51	76.56	85.65	75.56	84.86	80.21	88.16	78.56	86.94
+ SGF	74.63	84.29	70.51	80.98	80.28	88.35	78.48	87.08	83.59	90.53	80.98	88.68
+ SGF + Memory	<b>75.77</b>	<b>85.06</b>	<b>71.97</b>	<b>82.09</b>	<b>85.96</b>	<b>92.03</b>	<b>82.43</b>	<b>89.47</b>	<b>88.30</b>	<b>93.49</b>	<b>84.90</b>	<b>91.18</b>

### 3.5 Ablation Studies

**Scribble Generation strategy.** We evaluate four strategies (Sec. 2.7) on EndoVis 2018 and CholecSeg8k. Table 1 shows that contour-only performs best along all rounds, while centerline-only strokes lag, indicating boundary cues more effective for refinement.

**Component contribution.** Table 3 indicates that SGF yields consistent improvements over the baseline by injecting the latest correction into the memory-attention query, while Memory further boosts performance and its benefit becomes more evident in later rounds as correction history accumulates. Fig. 4 provides a qualitative view of these effects: SGF spatially diffuses the R1 correction scribble into the query features, while Memory Attention attends to the previous-round prediction stored in the memory bank and enhances features over relevant regions, leading to a refined mask.

## 4 Conclusion

We presented SCISSR, a scribble-promptable framework for interactive surgical segmentation. All added modules attach through standard embedding interfaces, enabling transfer to architectures such as SAM 3. Experiments on EndoVis 2018 and the out-of-distribution CholecSeg8k show that scribble prompts converge faster and more accurately than point or box. Future work will extend SCISSR to video-level annotation and validate usability with human annotators.

## A Iterative Refinement Algorithm

Algorithm 1 provides the complete pseudocode for the iterative refinement procedure described in Sec. 2.4. At each round the dual-track scribble encoder processes both the accumulated and the latest correction scribble, while the memory bank retains the previous round’s prediction to guide subsequent refinement.

---

### Algorithm 1 Iterative refinement with dual-track scribbles

---

```

1: Input: image  $I$ , initial scribble  $S_0$ , rounds  $T$ 
2:  $F_{\text{img}} \leftarrow \text{ImageEncoder}(I)$  (cached; frozen)
3:  $\mathcal{M} \leftarrow \emptyset$  (memory bank size 1)
4:  $S_{\text{acc}} \leftarrow S_0$ 
5: for  $t = 0$  to  $T - 1$  do
6:    $E_{\text{acc}} \leftarrow \text{ScribbleEnc}(S_{\text{acc}})$  (Track 1)
7:    $E_t \leftarrow \text{ScribbleEnc}(S_t)$  (Track 2; latest)
8:    $E_{\text{mask}} \leftarrow \begin{cases} \text{MaskEncoder}(\hat{M}_{t-1}), & t > 0 \\ \emptyset, & t = 0 \end{cases}$  (prev. mask prior)
9:    $F_q \leftarrow \text{SGF}(F_{\text{img}}, E_t)$ 
10:   $F_{\text{mem}} \leftarrow \text{MemAttn}(F_q, \mathcal{M})$  (no-mem embedding if  $\mathcal{M} = \emptyset$ )
11:   $\hat{M}_t \leftarrow \text{MaskDecoder}(F_{\text{mem}}, E_{\text{acc}} + E_{\text{mask}})$ 
12:   $\mathcal{M} \leftarrow \text{MemEncode}(F_{\text{img}}, \hat{M}_t)$ 
13:  Obtain next correction scribble  $S_{t+1}$  from user; update  $S_{\text{acc}} \leftarrow \max(S_{\text{acc}}, S_{t+1})$ 
14: end for
15: Output: refined mask  $\hat{M}_{T-1}$ 

```

---

## B Additional Comparison Tables

We provide extended comparison tables that complement the main results in Table 1. Table 4 reports class-average metrics on EndoVis 2018, while Tables 5 and 6 give sample-average and class-average breakdowns on CholecSeg8k (OOD), respectively.

**Table 4.** Class-average comparison on EndoVis 2018 (EndoVis 2018 test). All metrics (%) are averaged over  $C=10$  classes.  $Rk$  denotes the prediction after  $k$  refinement rounds.  $\Delta$  reports the cIoU gain from  $R0$  to  $R4$ .

Method	<b>R0</b>		<b>R2</b>		<b>R4</b>		$\Delta$ cIoU
	cIoU	cDice	cIoU	cDice	cIoU	cDice	
SCISSR (Adaptive)	72.08	82.18	84.84	91.09	86.89	92.47	+14.81
SCISSR (Contour only)	74.66	83.93	86.31	92.06	<b>87.92</b>	<b>93.05</b>	+13.26
SCISSR (Wave only)	69.74	80.36	84.99	91.19	86.67	92.26	+16.93
SCISSR (Centerline only)	71.37	81.82	82.20	89.41	83.29	90.08	+11.92
SAM2 Tiny (1pt/CC)	54.68	65.83	60.30	69.86	54.69	64.17	+0.01
SAM3 (1pt/CC)	53.28	64.36	57.82	67.05	51.89	59.83	-1.39

**Table 5.** Comparison on CholecSeg8k (CholecSeg8k test, OOD). Sample-average metrics (%) over  $N=8,800$  test masks.  $Rk$  denotes the prediction after  $k$  refinement rounds.  $\Delta$  reports the mIoU gain from  $R0$  to  $R2$ .

Method	<b>R0</b>		<b>R1</b>		<b>R2</b>		$\Delta$ mIoU
	mIoU	mDice	mIoU	mDice	mIoU	mDice	
SCISSR (Adaptive)	83.42	90.24	90.87	94.98	<b>92.30</b>	<b>95.82</b>	+8.88
SAM2 Tiny (1pt/CC)	62.18	72.30	63.09	74.33	62.18	73.44	+0.00
SAM3 (1pt/CC)	56.74	67.24	58.10	68.25	52.62	61.69	-4.12
SAM 2 Tiny (BBox)	76.22	84.62	-	-	-	-	-
SAM 3 (BBox)	77.85	85.78	-	-	-	-	-
MedSAM2 (BBox)	76.74	82.69	-	-	-	-	-

**Table 6.** Comparison on CholecSeg8k (CholecSeg8k test, OOD). Class-average metrics (%) over  $C=12$  classes.  $\Delta$  reports the cIoU gain from  $R0$  to  $R2$ .

Method	<b>R0</b>		<b>R1</b>		<b>R2</b>		$\Delta$ cIoU
	cIoU	cDice	cIoU	cDice	cIoU	cDice	
SCISSR (Adaptive)	80.58	87.96	87.63	92.77	<b>89.32</b>	<b>93.79</b>	+8.74
SAM2 Tiny (1pt/CC)	59.23	69.47	64.38	74.55	65.79	75.61	+6.56
SAM3 (1pt/CC)	58.71	67.96	61.75	70.92	56.27	65.91	-2.44
SAM 2 Tiny (BBox)	76.01	84.08	-	-	-	-	-
SAM 3 (BBox)	75.68	83.76	-	-	-	-	-
MedSAM2 (BBox)	75.36	81.35	-	-	-	-	-

## C Per-Class Detailed Results

Tables 7–10 report per-class IoU and Dice for each scribble strategy on EndoVis 2018 across all five rounds. Table 11 lists the corresponding per-class baseline numbers. Table 12 breaks down the component ablation by class. Tables 13–15 present per-class results on CholecSeg8k (OOD), and Table 16 reports convergence efficiency on CholecSeg8k.

**Table 7.** Per-class results of SCISSR on EndoVis 2018 (contour strategy). IoU and Dice (%) from Round 0 to Round 4.  $\Delta$  denotes the IoU gain from R0 to R4.

Class	$N$	R0		R1		R2		R3		R4		$\Delta$ IoU
		IoU	Dice									
<i>Instruments</i>												
Shaft	843	90.71	94.94	93.91	96.83	94.28	96.99	95.16	97.50	95.42	97.63	+4.71
Clasper	875	74.62	85.06	82.30	90.17	83.89	91.14	85.27	91.95	86.06	92.42	+11.44
Wrist	822	76.76	86.07	88.15	93.47	88.88	93.93	90.31	94.76	90.92	95.10	+14.16
<i>Tissues</i>												
Kidney parenchyma	949	82.40	89.42	93.25	96.44	94.27	97.00	94.95	97.37	95.39	97.61	+12.99
Covered kidney	484	73.65	84.31	92.86	96.27	94.48	97.15	95.13	97.50	95.80	97.85	+22.15
Small intestine	225	90.73	94.94	94.02	96.84	94.57	97.14	95.26	97.52	95.85	97.85	+5.12
<i>Other</i>												
Thread	102	57.05	72.22	67.78	80.59	68.01	80.74	68.25	80.89	68.29	80.89	+11.24
Clamps	69	75.72	85.47	83.75	90.81	86.93	92.86	88.74	93.97	88.48	93.84	+12.76
Suturing needle	95	44.54	58.41	65.45	77.29	65.99	77.98	67.95	79.44	69.46	80.72	+24.92
Ultrasound probe	152	80.41	88.50	89.97	94.61	91.79	95.65	93.24	96.45	93.54	96.58	+13.13

**Table 8.** Per-class results of SCISSR on EndoVis 2018 (adaptive strategy). IoU and Dice (%) from Round 0 to Round 4.  $\Delta$  denotes the IoU gain from R0 to R4.

Class	$N$	R0		R1		R2		R3		R4		$\Delta$ IoU
		IoU	Dice									
<i>Instruments</i>												
Shaft	843	86.38	92.39	92.13	95.83	93.58	96.64	94.20	96.98	94.50	97.14	+8.12
Clasper	875	71.43	82.88	81.37	89.58	83.43	90.84	84.41	91.41	85.26	91.95	+13.83
Wrist	822	70.12	81.35	84.43	91.14	87.46	93.03	88.68	93.75	89.57	94.31	+19.45
<i>Tissues</i>												
Kidney parenchyma	949	79.86	87.83	90.01	94.56	91.88	95.62	92.76	96.12	93.32	96.43	+13.46
Covered kidney	484	70.28	81.91	83.18	90.38	88.37	93.57	90.59	94.86	92.25	95.81	+21.97
Small intestine	225	85.73	91.99	92.08	95.76	93.31	96.45	94.28	97.00	94.92	97.33	+9.19
<i>Other</i>												
Thread	102	58.52	73.45	67.79	80.62	68.62	81.20	68.83	81.35	68.80	81.32	+10.28
Clamps	69	73.22	82.66	82.85	89.34	84.16	90.12	85.27	91.10	87.40	92.92	+14.18
Suturing needle	95	45.31	59.14	62.76	74.82	66.59	78.26	69.04	80.51	70.15	81.35	+24.84
Ultrasound probe	152	79.95	88.21	89.00	93.98	91.04	95.19	92.18	95.85	92.76	96.18	+12.81

**Table 9.** Per-class results of SCISSR on EndoVis 2018 (wave-only strategy). IoU and Dice (%) from Round 0 to Round 4.  $\Delta$  denotes the IoU gain from R0 to R4.

Class	N	R0		R1		R2		R3		R4		$\Delta$ IoU
		IoU	Dice									
<i>Instruments</i>												
Shaft	843	84.54	91.30	91.91	95.72	93.45	96.57	94.04	96.88	94.46	97.10	+9.92
Clasper	875	68.72	80.98	80.09	88.74	82.89	90.53	84.19	91.33	84.77	91.66	+16.05
Wrist	822	67.49	79.49	83.63	90.60	87.26	92.91	88.36	93.58	89.01	93.98	+21.52
<i>Tissues</i>												
Kidney parenchyma	949	78.54	86.99	90.23	94.74	92.82	96.21	93.74	96.72	94.26	97.00	+15.72
Covered kidney	484	67.40	79.78	88.14	93.64	91.49	95.52	93.58	96.66	94.58	97.19	+27.18
Small intestine	225	84.89	91.55	92.78	96.17	94.18	96.94	94.74	97.25	95.15	97.48	+10.26
<i>Other</i>												
Thread	102	50.83	66.80	63.14	77.07	66.98	80.04	68.26	80.97	68.81	81.35	+17.98
Clamps	69	70.62	79.96	81.22	88.24	83.24	90.05	83.87	90.47	84.12	90.62	+13.50
Suturing needle	95	45.51	59.48	63.46	75.66	65.86	77.57	66.91	78.52	68.36	79.75	+22.85
Ultrasound probe	152	78.82	87.24	89.84	94.51	91.77	95.60	92.73	96.19	93.21	96.44	+14.39

**Table 10.** Per-class results of SCISSR on EndoVis 2018 (centerline-only strategy). IoU and Dice (%) from Round 0 to Round 4.  $\Delta$  denotes the IoU gain from R0 to R4.

Class	N	R0		R1		R2		R3		R4		$\Delta$ IoU
		IoU	Dice									
<i>Instruments</i>												
Shaft	843	85.33	91.69	91.07	95.22	92.54	96.05	93.08	96.34	93.46	96.55	+8.13
Clasper	875	71.03	82.58	79.54	88.30	80.85	89.08	81.30	89.33	81.45	89.41	+10.42
Wrist	822	67.02	79.38	79.93	88.25	82.70	89.96	83.56	90.47	83.95	90.70	+16.93
<i>Tissues</i>												
Kidney parenchyma	949	77.85	86.46	88.23	93.52	89.75	94.35	90.36	94.67	90.65	94.81	+12.80
Covered kidney	484	66.93	79.28	75.88	85.58	80.37	88.52	82.95	90.16	84.67	91.22	+17.74
Small intestine	225	85.16	91.67	91.11	95.24	92.65	96.11	93.39	96.51	93.79	96.73	+8.63
<i>Other</i>												
Thread	102	59.01	73.83	67.74	80.54	68.59	81.19	68.95	81.44	68.79	81.33	+9.78
Clamps	69	75.84	85.55	82.71	90.17	83.19	90.32	83.38	90.45	83.33	90.43	+7.49
Suturing needle	95	45.86	59.74	60.05	72.52	62.94	74.99	63.68	75.62	64.06	76.02	+18.20
Ultrasound probe	152	79.68	88.05	87.53	92.97	88.45	93.47	88.65	93.58	88.76	93.64	+9.08

**Table 11.** Per-class results of baselines on EndoVis 2018. IoU (%) from Round 0 to Round 4 for iterative methods; single-round IoU and Dice for box methods.

Class	N	SAM2 Tiny (1pt/CC) IoU					SAM3 (1pt/CC) IoU					SAM 2 Tiny (BBox)		SAM 3 (BBox)		MedSAM2 (BBox)	
		R0	R1	R2	R3	R4	R0	R1	R2	R3	R4	IoU	Dice	IoU	Dice	IoU	Dice
<i>Instruments</i>																	
Shaft	843	70.52	77.03	77.06	73.32	67.08	69.99	74.09	70.40	62.25	53.81	64.98	73.19	67.11	74.53	72.78	82.25
Clasper	875	44.65	54.05	52.87	46.95	39.08	55.54	57.10	54.82	49.19	42.66	45.04	55.58	58.17	68.72	52.58	67.12
Wrist	822	54.56	65.58	70.06	71.21	70.36	55.57	63.38	69.02	71.80	72.10	67.54	76.50	71.29	80.07	65.30	76.22
<i>Tissues</i>																	
Kidney parenchyma	949	63.64	63.38	60.87	58.56	56.21	61.22	58.96	53.66	48.45	43.72	76.59	85.00	80.58	88.18	15.02	19.40
Covered kidney	484	43.86	47.46	45.83	41.97	38.53	39.95	44.23	42.69	39.07	35.37	59.78	71.95	59.86	72.35	10.11	13.57
Small intestine	225	65.73	81.15	82.96	80.47	76.34	64.35	79.16	80.16	73.53	66.99	87.40	92.45	88.67	93.60	50.04	57.10
<i>Other</i>																	
Thread	102	22.48	9.77	5.82	3.44	2.29	8.87	6.15	2.54	1.59	1.47	17.72	26.18	32.46	44.27	1.43	2.56
Clamps	69	83.38	87.07	87.49	87.58	87.18	77.51	82.54	85.44	86.26	86.65	86.86	92.60	87.21	92.82	75.74	85.56
Suturing needle	95	35.79	42.88	47.78	51.68	51.96	38.10	41.75	41.80	44.56	43.76	50.63	63.35	57.79	69.95	27.67	38.60
Ultrasound probe	152	62.19	71.77	72.22	67.52	57.88	61.68	74.85	77.64	77.31	72.34	81.23	88.53	84.33	90.69	80.80	88.03

**Table 12.** Component ablation per-class on EndoVis 2018. IoU (%) at R0 and R2 for each configuration.  $\Delta$  denotes the IoU gain from Baseline to SGF+Memory at R2.

Class	$N$	Baseline		+ SGF		+ SGF + Memory		$\Delta$ IoU
		R0	R2	R0	R2	R0	R2	
<i>Instruments</i>								
Shaft	843	81.75	89.02	87.20	91.53	86.22	93.40	+4.38
Clasper	875	60.01	73.76	70.19	78.16	71.11	83.39	+9.63
Wrist	822	59.64	73.35	66.26	78.55	69.96	87.55	+14.20
<i>Tissues</i>								
Kidney parenchyma	949	77.26	84.75	79.92	88.12	79.83	91.20	+6.45
Covered kidney	484	65.36	78.98	69.63	81.90	69.78	87.92	+8.94
Small intestine	225	83.45	90.78	85.44	92.24	87.04	93.72	+2.94
<i>Other</i>								
Thread	102	63.11	66.52	55.63	65.69	57.56	68.45	+1.93
Clamps	69	76.53	82.02	73.35	83.76	74.22	85.29	+3.27
Suturing needle	95	53.19	60.12	40.08	62.13	44.65	66.19	+6.07
Ultrasound probe	152	76.48	86.32	77.45	87.75	79.30	91.07	+4.75

**Table 13.** Per-class results of SAM2 Tiny (10pt/ch) on CholecSeg8k (OOD). IoU and Dice (%) from Round 0 to Round 2.  $\Delta$  denotes the IoU gain from R0 to R2.

Class	$N$	R0		R1		R2		$\Delta$ IoU
		IoU	Dice	IoU	Dice	IoU	Dice	
<i>Tissues / Organs</i>								
Abdominal Wall	1464	71.44	81.60	80.96	88.12	81.92	88.52	+10.48
Liver	1679	67.43	78.46	72.06	82.18	74.49	83.83	+7.06
Gastrointestinal Tract	941	61.84	71.81	68.16	77.26	70.54	78.92	+8.70
Fat	1519	56.59	68.70	70.36	80.07	73.18	81.45	+16.59
Connective Tissue	240	53.89	67.37	57.54	71.23	62.34	75.21	+8.45
Gallbladder	1279	70.91	80.03	72.94	81.64	75.71	83.71	+4.80
Hepatic Vein	77	45.24	60.46	39.12	52.83	28.52	40.06	-16.72
Liver Ligament	80	94.63	97.21	95.46	97.67	95.36	97.62	+0.73
Cystic Duct	1	96.75	98.35	95.02	97.45	95.90	97.91	-0.85
<i>Instruments</i>								
Grasper	1080	78.52	87.35	76.46	85.52	75.80	84.19	-2.72
L-hook Electrocautery	360	89.22	93.87	88.57	93.29	89.37	93.65	+0.15
<i>Other</i>								
Blood	80	20.79	33.28	23.49	37.48	23.10	36.63	+2.31

**Table 14.** Per-class results on CholecSeg8k (Adaptive strategy, OOD). IoU and Dice (%) from Round 0 to Round 2.  $\Delta$  denotes the IoU gain from R0 to R2.

Class	N	R0		R1		R2		$\Delta$ IoU
		IoU	Dice	IoU	Dice	IoU	Dice	
<i>Tissues / Organs</i>								
Abdominal Wall	1464	86.61	92.25	94.35	96.97	95.71	97.75	+9.10
Liver	1679	86.79	92.72	93.66	96.70	95.14	97.50	+8.35
Gastrointestinal Tract	941	77.03	86.07	88.31	93.60	89.47	94.29	+12.44
Fat	1519	86.89	92.80	93.27	96.47	94.91	97.36	+8.02
Connective Tissue	240	79.13	88.03	87.36	93.15	90.52	94.97	+11.39
Gallbladder	1279	78.79	86.50	89.01	93.75	90.32	94.63	+11.53
Hepatic Vein	77	41.00	57.49	54.34	69.50	58.58	72.33	+17.58
Liver Ligament	80	96.61	98.28	97.38	98.67	97.74	98.85	+1.13
Cystic Duct	1	96.26	98.10	97.82	98.90	98.12	99.05	+1.86
<i>Instruments</i>								
Grasper	1080	82.26	89.97	86.07	92.35	87.33	93.11	+5.07
L-hook Electrocautery	360	89.55	93.81	92.98	96.17	93.35	96.38	+3.80
<i>Other</i>								
Blood	80	66.07	79.54	77.07	86.98	80.60	89.19	+14.53

**Table 15.** Per-class results of baselines on CholecSeg8k (OOD). IoU (%) from Round 0 to Round 2 for iterative methods; single-round IoU for box methods.  $\Delta$  denotes the IoU change from R0 to R2.

Class	N	SAM2 Tiny (1pt/CC)			SAM3 (1pt/CC)			SAM 2 Tiny (BBox)		SAM 3 (BBox)		MedSAM2 (BBox)	
		R0	R1	R2	R0	R1	R2	IoU	Dice	IoU	Dice	IoU	Dice
<i>Tissues / Organs</i>													
Abdominal Wall	1464	66.15	63.21	61.81	51.20	46.91	35.26	81.38	88.35	85.08	90.85	80.39	85.81
Liver	1679	62.88	54.35	47.93	51.05	46.67	32.51	72.76	82.44	75.80	84.83	73.61	80.41
Gastrointestinal Tract	941	56.67	63.12	69.92	61.20	69.80	72.35	82.04	89.53	82.58	90.09	85.82	91.81
Fat	1519	49.51	54.14	52.09	42.76	43.92	38.56	64.36	75.15	65.65	76.27	60.48	65.83
Connective Tissue	240	47.45	53.42	51.39	45.16	54.38	54.43	72.24	83.07	56.68	71.28	88.21	93.59
Gallbladder	1279	67.78	70.00	69.24	66.06	71.45	70.98	82.34	88.81	82.38	88.24	87.80	93.05
Hepatic Vein	77	31.81	50.26	66.70	27.93	42.74	51.81	63.90	77.60	62.63	76.51	57.65	72.60
Liver Ligament	80	95.36	92.57	90.68	86.44	84.92	72.79	97.16	98.56	97.09	98.52	95.88	97.89
Cystic Duct	1	59.22	86.67	92.97	94.74	96.38	65.16	97.53	98.75	97.57	98.77	96.99	98.47
<i>Instruments</i>													
Grasper	1080	70.08	76.20	77.68	73.31	77.79	77.44	77.46	86.14	82.11	89.74	75.82	83.15
L-hook Electrocautery	360	85.79	89.43	90.30	85.90	88.21	87.60	91.77	95.61	92.24	95.88	91.68	95.58
<i>Other</i>													
Blood	80	18.01	19.22	18.80	18.72	17.88	16.37	29.15	45.00	28.36	44.09	9.97	18.01

**Table 16.** Convergence efficiency on CholecSeg8k (CholecSeg8k, OOD). Success rate (%) is the fraction of  $N=8,800$  test masks reaching the Dice threshold within 4 rounds. Mean rounds is averaged over successful masks only.

Method	Dice $\geq$	Success (%)	Mean Rnd	Cumulative % by round				
				R0	R1	R2	R3	R4
SCISSR (Adaptive)	0.75	<b>99.4</b>	<b>1.28</b>	78.2	94.8	98.0	99.1	99.4
	0.85	<b>98.0</b>	<b>1.50</b>	62.4	88.6	94.8	97.1	98.0
	0.90	<b>94.0</b>	<b>1.73</b>	47.4	79.3	88.6	92.2	94.0
SAM2 Tiny (1pt/CC)	0.75	79.9	1.37	61.8	72.5	77.0	79.1	79.9
	0.85	64.8	1.51	44.8	56.2	61.1	63.7	64.8
	0.90	49.8	1.61	32.9	41.3	46.2	48.6	49.8
SAM3 (1pt/CC)	0.75	65.8	1.31	52.1	61.4	64.0	65.2	65.8
	0.85	53.8	1.47	38.1	47.6	51.4	53.0	53.8
	0.90	42.8	1.53	29.4	36.9	40.3	41.9	42.8

## D Point Prompt Density Analysis

To investigate whether simply increasing the number of point prompts can close the gap with scribble prompts, we vary the point density from 1 to 50 per channel on a subset of CholecSeg8k (4 videos). As shown in Table 17, both SAM 2 Tiny and SAM 3 peak at 10 points and degrade sharply beyond that, confirming that the point interface cannot exploit denser spatial signals.

**Table 17.** Effect of point prompt density on SAM 2 Tiny and SAM 3 (CholecSeg8k, 4 videos, Round 2). Performance degrades sharply beyond 10 points per channel.

Method	1 pt		10 pts		30 pts		50 pts	
	IoU	Dice	IoU	Dice	IoU	Dice	IoU	Dice
SAM 2 Tiny	60.25	71.79	<b>73.76</b>	<b>82.49</b>	34.36	44.24	22.43	30.84
SAM 3	50.29	60.14	61.46	72.79	1.12	1.55	0.00	0.00

## E Scribble Strategy Ablation

Fig. 5 visualizes the four scribble generation strategies evaluated in Sec. 3.5. Contour-based scribbles consistently achieve the highest mIoU and mDice at both R0 and R4, while centerline-only lags due to the absence of boundary cues.

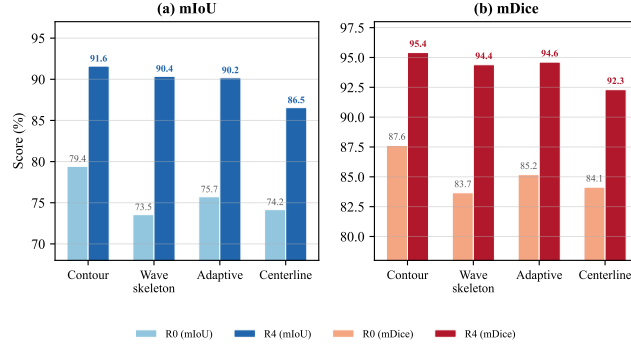


**Fig. 5.** Scribble strategy ablation on EndoVis 2018. Contour achieves the best R0 and R4 across both mIoU and mDice.

## F Additional Figures

We include supplementary visualizations that complement the main-text analysis. Fig. 6 plots the iterative refinement curves corresponding to Table 1. Fig. 7 shows cumulative success rates at three Dice thresholds. Fig. 8 illustrates the point prompt degradation discussed in Sec. 3.4. Fig. 9 visualizes the component ablation from Table 3.

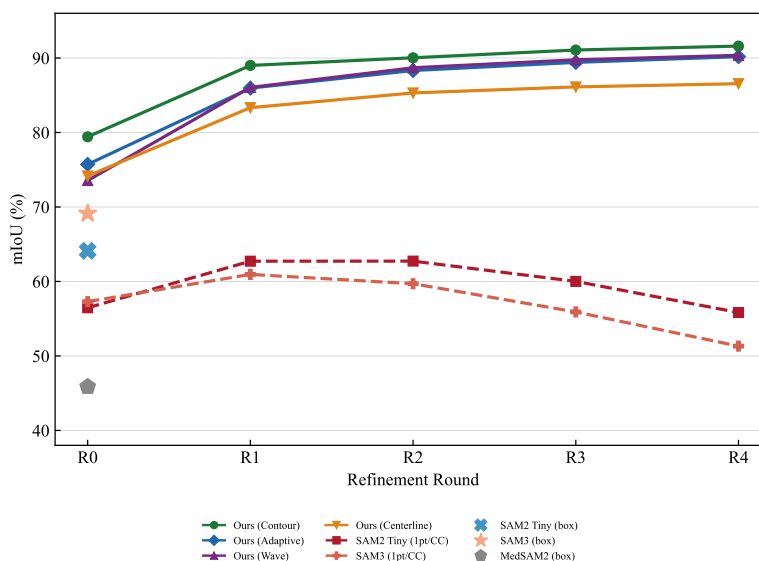


**Fig. 6.** Iterative refinement curves on EndoVis 2018. This figure visualizes the same mIoU data reported in Table 1. All four scribble strategies improve steadily across rounds, while point-based methods (SAM2 Tiny, SAM3) degrade after R1. Box baselines (markers at R0) cannot iterate.

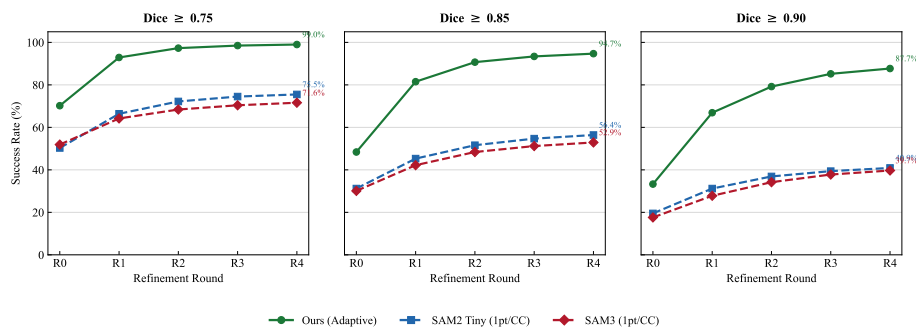


**Fig. 7.** Cumulative success rate on EndoVis 2018 at three Dice thresholds. Our method converges to high-quality masks within 1–2 rounds for most samples, while point-based methods plateau early.

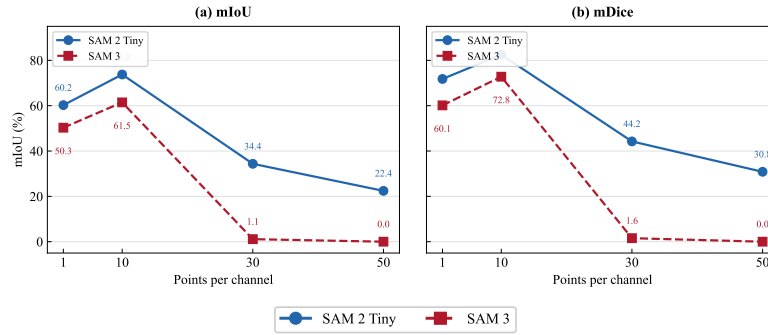


**Fig. 8.** Point prompt degradation on CholecSeg8k. Both SAM 2 Tiny and SAM 3 peak at 10 points and collapse beyond 30, confirming that the point interface cannot exploit denser spatial signals.

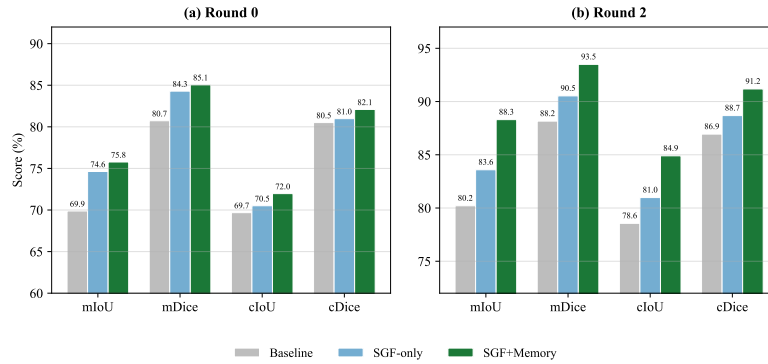


**Fig. 9.** Component ablation on EndoVis 2018. Each module (SGF, Memory) contributes additive gains at both R0 and R2 across all four metrics. Numeric values are in Table 3.

## References

1. Allan, M., Kondo, S., Bodenstedt, S., Leger, S., Kadkhodamohammadi, R., Luengo, I., Fuentes, F., Flouty, E., Mohammed, A., Pedersen, M., et al.: 2018 robotic scene segmentation challenge. arXiv preprint arXiv:2001.11190 (2020)
2. Carion, N., Gustafson, L., Hu, Y.T., Debnath, S., Hu, R., Suris, D., Ryali, C., Alwala, K.V., Khedr, H., Huang, A., et al.: Sam 3: Segment anything with concepts. arXiv preprint (2025)
3. Cheng, J., Ye, J., Deng, Z., Chen, J., Li, T., Wang, H., Su, Y., Huang, Z., Chen, J., Jiang, L., et al.: Sam-med2d. arXiv preprint arXiv:2308.16184 (2023)

4. Guo, M.H., Lu, C.Z., Hou, Q., Liu, Z.N., Cheng, M.M., Hu, S.M.: SegNeXt: Rethinking convolutional attention design for semantic segmentation. In: *Advances in Neural Information Processing Systems (NeurIPS)*. vol. 35, pp. 1140–1156 (2022)
5. Hong, W.Y., Kao, C.L., Kuo, Y.H., Wang, J.R., Chang, W.L., Shih, C.S.: Cholec-Seg8k: A semantic segmentation dataset for laparoscopic cholecystectomy based on Cholec80. *arXiv preprint arXiv:2012.12453* (2020)
6. Hu, E.J., Shen, Y., Wallis, P., Allen-Zhu, Z., Li, Y., Wang, S., Wang, L., Chen, W.: Lora: Low-rank adaptation of large language models. In: *International Conference on Learning Representations (ICLR)* (2022)
7. Jin, Y., Yu, Y., Chen, C., Zhao, Z., Heng, P.A., Stoyanov, D.: Exploring intra- and inter-video relation for surgical semantic scene segmentation. *IEEE Transactions on Medical Imaging* **41**(11), 2991–3002 (2022)
8. Kamtam, D.N., Shrager, J.B., Malla, S.D., Wang, X., Lin, N., Cardona, J.J., Yeung-Levy, S., Hu, C.: A fine-tuned foundational model SurgiSAM2 for surgical video anatomy segmentation and detection. *Scientific Reports* **15**, 35961 (2025)
9. Kirillov, A., Mintun, E., Ravi, N., Mao, H., Rolber, C., Gustafson, L., Xiao, T., Whitehead, S., Berg, A.C., Lo, W.Y., Dollár, P., Girshick, R.: Segment anything. In: *Proceedings of the IEEE/CVF International Conference on Computer Vision (ICCV)*. pp. 4015–4026 (2023)
10. Lin, D., Dai, J., Jia, J., He, K., Sun, J.: Scribblesup: Scribble-supervised convolutional networks for semantic segmentation. In: *Proceedings of the IEEE/CVF Conference on Computer Vision and Pattern Recognition (CVPR)*. pp. 3159–3167 (2016)
11. Liu, M., Han, Y., Wang, J., Wang, C., Wang, Y., Meijering, E.: LSKANet: Long strip kernel attention network for robotic surgical scene segmentation. *IEEE Transactions on Medical Imaging* **43**(4), 1308–1320 (2024)
12. Liu, Q., Xu, Z., Bertasius, G., Niethammer, M.: Simpleclick: Interactive image segmentation with simple vision transformers. In: *Proceedings of the IEEE/CVF International Conference on Computer Vision (ICCV)*. pp. 22290–22300 (2023)
13. Luo, X., Wang, G., Song, T., Zhang, J., Aertsen, M., Deprest, J., Ourselin, S., Vercauteren, T., Zhang, S.: MIDeepSeg: Minimally interactive segmentation of unseen objects from medical images using deep learning. *Medical Image Analysis* **72**, 102102 (2021)
14. Ma, J., He, Y., Li, F., Han, L., You, C., Wang, B.: Segment anything in medical images. *Nature Communications* **15**, 654 (2024)
15. Ma, J., Yang, Z., Kim, S., Chen, B., Baharoon, M., Fallahpour, A., Asakereh, R., Lyu, H., Wang, B.: Medsam2: Segment anything in 3d medical images and videos. *ArXiv abs/2504.03600* (2025), <https://api.semanticscholar.org/CorpusID:277596374>
16. Ravi, N., Gabber, V., Hu, Y.T., Hu, R., Ryali, C., Ma, T., Khedr, H., Rädle, R., Rolber, C., Gustafson, L., et al.: Sam 2: Segment anything in images and videos. *arXiv preprint arXiv:2408.00714* (2024)
17. Ronneberger, O., Fischer, P., Brox, T.: U-Net: Convolutional networks for biomedical image segmentation. In: *Medical Image Computing and Computer Assisted Intervention (MICCAI)*. LNCS, vol. 9351, pp. 234–241. Springer (2015)
18. Sofiiuk, K., Petrov, I., Barinova, O., Konushin, A.: f-brs: Rethinking backpropagating refinement for interactive segmentation. In: *Proceedings of the IEEE/CVF Conference on Computer Vision and Pattern Recognition (CVPR)*. pp. 8623–8632 (2020)

19. Sofiiuk, K., Petrov, I.A., Konushin, A.: Reviving iterative training with mask guidance for interactive segmentation. In: IEEE International Conference on Image Processing (ICIP). pp. 3141–3145 (2022)
20. Tang, M., Perazzi, F., Djelouah, A., Ben Ayed, I., Schroers, C., Boykov, Y.: On regularized losses for weakly-supervised CNN segmentation. In: Proceedings of the European Conference on Computer Vision (ECCV). pp. 507–522 (2018)
21. Wang, G., Zuluaga, M.A., Li, W., Pratt, R., Patel, P.A., Aertsen, M., Doel, T., David, A.L., Deprest, J., Ourselin, S., Vercauteren, T.: DeepIGeoS: A deep interactive geodesic framework for medical image segmentation. IEEE Transactions on Pattern Analysis and Machine Intelligence **41**(7), 1559–1572 (2019)
22. Wang, J., Sun, K., Cheng, T., Jiang, B., Deng, C., Zhao, Y., Liu, D., Mu, Y., Tan, M., Wang, X., Liu, W., Xiao, B.: Deep high-resolution representation learning for visual recognition. IEEE Transactions on Pattern Analysis and Machine Intelligence **43**(10), 3349–3364 (2021)
23. Wong, H.E., Rakic, M., Gutttag, J., Dalca, A.V.: ScribblePrompt: Fast and flexible interactive segmentation for any biomedical image. In: Proceedings of the European Conference on Computer Vision (ECCV). pp. 207–225 (2024)
24. Xiao, T., Liu, Y., Zhou, B., Jiang, Y., Sun, J.: Unified perceptual parsing for scene understanding. In: Proceedings of the European Conference on Computer Vision (ECCV). pp. 418–434 (2018)
25. Xie, E., Wang, W., Yu, Z., Anandkumar, A., Alvarez, J.M., Luo, P.: SegFormer: Simple and efficient design for semantic segmentation with transformers. In: Advances in Neural Information Processing Systems (NeurIPS). pp. 12077–12090 (2021)
26. Xu, N., Price, B., Cohen, S., Yang, J., Huang, T.: Deep interactive object selection. In: Proceedings of the IEEE/CVF Conference on Computer Vision and Pattern Recognition (CVPR). pp. 373–381 (2016)
27. Yuan, C., Ban, Y.: Surgical scene segmentation by transformer with asymmetric feature enhancement. In: 2025 IEEE 22nd International Symposium on Biomedical Imaging (ISBI). pp. 1–5. IEEE (2025)
28. Yuan, C., Jiang, J., Yang, K., et al.: Systematic evaluation and guidelines for segment anything model in surgical video analysis. arXiv preprint arXiv:2501.00525 (2024)
29. Yue, W., Zhang, J., Hu, K., Xia, Y., Luo, J., Wang, Z.: SurgicalSAM: Efficient class promptable surgical instrument segmentation. In: AAAI Conference on Artificial Intelligence. pp. 6890–6898 (2024)
30. Zhang, K., Zhuang, X.: CycleMix: A holistic strategy for medical image segmentation from scribble supervision. In: Proceedings of the IEEE/CVF Conference on Computer Vision and Pattern Recognition (CVPR). pp. 11656–11665 (2022)